

## RESEARCH ARTICLE

# $B_1$ inhomogeneity correction of RARE MRI at low SNR: Quantitative in vivo $^{19}\text{F}$ MRI of mouse neuroinflammation with a cryogenically-cooled transceive surface radiofrequency probe

Paula Ramos Delgado<sup>1,2</sup>   | Andre Kuehne<sup>3</sup>  | Mariya Aravina<sup>1</sup>  |  
 Jason M. Millward<sup>1</sup>  | Alonso Vázquez<sup>3</sup>  | Ludger Starke<sup>1</sup>  |  
 Helmar Waiczies<sup>3</sup>  | Andreas Pohlmann<sup>1</sup>  | Thoralf Niendorf<sup>1,2,3</sup>  |  
 Sonia Waiczies<sup>1</sup> 

<sup>1</sup>Max-Delbrück-Center for Molecular Medicine in the Helmholtz Association (MDC), Berlin Ultrahigh Field Facility, Berlin, Germany

<sup>2</sup>Experimental and Clinical Research Center, a cooperation between the Max-Delbrück-Center for Molecular Medicine in the Helmholtz Association and the Charité-Universitätsmedizin Berlin, Berlin, Germany

<sup>3</sup>MRI.TOOLS, Berlin, Germany

## Correspondence

Paula Ramos Delgado, Berlin Ultrahigh Field Facility, Max Delbrück Center for Molecular Medicine in the Helmholtz Association, Robert-Rössle-Str. 10, 13125 Berlin, Germany.

Email: Paula.Ramos@mdc-berlin.de

## Funding information

The German Research Foundation (Deutsche Forschungsgemeinschaft [DFG]); Grant/Award Nos. DFG-PO1869, DFG-WA2804, and Projektnummer 394046635, SFB 1365, RENOPROTECTION

**Purpose:** Low SNR in fluorine-19 ( $^{19}\text{F}$ ) MRI benefits from cryogenically-cooled transceive surface RF probes (CRPs), but strong  $B_1$  inhomogeneities hinder quantification. Rapid acquisition with refocused echoes (RARE) is an SNR-efficient method for MRI of neuroinflammation with perfluorinated compounds but lacks an analytical signal intensity equation to retrospectively correct  $B_1$  inhomogeneity. Here, a workflow was proposed and validated to correct and quantify  $^{19}\text{F}$ -MR signals from the inflamed mouse brain using a  $^{19}\text{F}$ -CRP.

**Methods:** In vivo  $^{19}\text{F}$ -MR images were acquired in a neuroinflammation mouse model with a quadrature  $^{19}\text{F}$ -CRP using an imaging setup including 3D-printed components to acquire co-localized anatomical and  $^{19}\text{F}$  images. *Model-based corrections* were validated on a uniform  $^{19}\text{F}$  phantom and in the neuroinflammatory model. Corrected  $^{19}\text{F}$ -MR images were benchmarked against reference images and overlaid on in vivo  $^1\text{H}$ -MR images. Computed concentration uncertainty maps using Monte Carlo simulations served as a measure of performance of the  $B_1$  corrections.

**Results:** Our study reports on the first quantitative in vivo  $^{19}\text{F}$ -MR images of an inflamed mouse brain using a  $^{19}\text{F}$ -CRP, including in vivo  $T_1$  calculations for  $^{19}\text{F}$ -nanoparticles during pathology and  $B_1$  corrections for  $^{19}\text{F}$ -signal quantification. *Model-based corrections* markedly improved  $^{19}\text{F}$ -signal quantification from errors > 50% to < 10% in a uniform phantom ( $p < 0.001$ ). Concentration uncertainty maps ex vivo and in vivo yielded uncertainties that were generally < 25%.

This is an open access article under the terms of the Creative Commons Attribution-NonCommercial License, which permits use, distribution and reproduction in any medium, provided the original work is properly cited and is not used for commercial purposes.

© 2021 The Authors. *Magnetic Resonance in Medicine* published by Wiley Periodicals LLC on behalf of International Society for Magnetic Resonance in Medicine.

Monte Carlo simulations prescribed  $\text{SNR} \geq 10.1$  to reduce uncertainties  $< 10\%$ , and  $\text{SNR} \geq 4.25$  to achieve uncertainties  $< 25\%$ .

**Conclusion:** Our *model-based correction* method facilitated  $^{19}\text{F}$  signal quantification in the inflamed mouse brain when using the SNR-boosting  $^{19}\text{F}$ -CRP technology, paving the way for future low-SNR  $^{19}\text{F}$ -MRI applications in vivo.

#### KEYWORDS

$^{19}\text{F}$ -MRI,  $B_1$  correction, inflammation, RARE, transceive surface RF probe

## 1 | INTRODUCTION

Fluorine-19 ( $^{19}\text{F}$ ) MRI shows promise in several biomedical applications.<sup>1–3</sup> However,  $^{19}\text{F}$ -MRI suffers from low SNR due to the very limited availability of  $^{19}\text{F}$  nuclei in vivo. Consequently,  $^{19}\text{F}$ -MRI is constrained by long measurements. One SNR-boosting strategy has been to implement sensitivity-promoting surface RF coil technologies.<sup>4</sup> Cryogenically cooled transceive surface RF probes (CRPs) have introduced a paradigm shift in preclinical imaging, providing substantial SNR gains compared with room-temperature RF coils.<sup>5–10</sup> Further increases in SNR have been achieved with quadrature configurations, which provide a  $\sqrt{2}$  SNR gain and better transversal  $B_1$  homogeneity compared with linear polarized RF coils.<sup>11–13</sup>

Quadrature CRPs are typically single-tuned for X-nuclei,<sup>8</sup> since dual-tunable capabilities would require electromagnetic decoupling between coil elements,<sup>14–16</sup> degrading signal sensitivity. This adds extra post-processing challenges when locating quantified  $^{19}\text{F}$  signals in vivo. Moreover, the low-SNR and sparse nature of  $^{19}\text{F}$  prevents the MR system from performing reference power adjustments without an external  $^{19}\text{F}$  reference.

The greatest challenge of transceive surface RF probes like the  $^{19}\text{F}$ -CRP is their strong  $B_1$  inhomogeneities,<sup>4,17</sup> which hamper  $T_1$  contrast and signal quantification, as the measured  $^{19}\text{F}$  signal depends on the number of  $^{19}\text{F}$  atoms per pixel, their distance from the probe surface, and relaxation times. Inhomogeneities in the excitation field ( $B_1^+$ ) are typically corrected retrospectively using signal-intensity (SI) equations of corresponding RF pulse sequences. This is possible for gradient-echo or spin-echo techniques,<sup>18–20</sup> but the SNR-efficient rapid acquisition with refocused echoes (RARE) technique lacks an exact SI equation.<sup>21,22</sup> We previously implemented three  $B_1$  correction methods (*model-based*, *hybrid*, and *sensitivity*) for RARE  $^1\text{H}$ -MRI and transceive surface RF probes, considerably increasing image homogeneity and significantly reducing errors in signal quantification and  $T_1$  contrast.<sup>23</sup>

The low SNR, signal sparsity, and lack of a priori location of the  $^{19}\text{F}$  signal constrain the reliability of signal

quantification, even after  $B_1$  correction. A procedure that evaluates the quality of the SI correction and quantification per image voxel is thus crucial. This is particularly relevant when monitoring and quantifying inflammation e.g., in the animal model of multiple sclerosis (MS), experimental autoimmune encephalomyelitis (EAE)<sup>24,25</sup> using  $^{19}\text{F}$ -nanoparticles (NPs).

Here, we implemented and validated our  $B_1$  correction approaches<sup>23</sup> to correct  $^{19}\text{F}$ -MR images from a single-tuned quadrature  $^{19}\text{F}$ -CRP after estimating in vivo  $T_1$  of  $^{19}\text{F}$ -NPs in the EAE brain using a volume resonator. We performed Monte Carlo SNR simulations to estimate the associated concentration uncertainty. We also established a workflow using 3D-printed add-ons to facilitate in vivo localization of  $^{19}\text{F}$ -MR images from the  $^{19}\text{F}$ -CRP on anatomical images acquired from a  $^1\text{H}$  volume resonator. This workflow and correction method delivered the first quantitative in vivo  $^{19}\text{F}$ -MR images of an inflamed EAE mouse brain using a  $^{19}\text{F}$ -CRP. These results will be pivotal to drive future  $^{19}\text{F}$  research using transceive surface RF technologies to quantify inflammation or  $^{19}\text{F}$ -compounds in in vivo studies.

## 2 | METHODS

### 2.1 | Magnetic resonance hardware

All experiments were carried out on a 9.4T small animal MR scanner (BioSpec 94/20; Bruker BioSpin, Ettlingen, Germany).

$^{19}\text{F}$  images were acquired using a  $^{19}\text{F}$  cryogenically-cooled transceive surface RF probe ( $^{19}\text{F}$ -CRP CryoProbe; Bruker BioSpin)<sup>17</sup> for mouse head imaging (inner diameter [ID] = 20 mm), composed of two elements operating in quadrature mode. Anatomical images were measured using a 72-mm (ID) linear volume resonator (Bruker BioSpin).  $T_1$  measurements of  $^{19}\text{F}$ -NPs in EAE brains and reference  $^{19}\text{F}$  images were acquired using a small-diameter (ID = 18.4 mm) mouse head  $^1\text{H}/^{19}\text{F}$  volume resonator.<sup>26</sup>

## 2.2 | Anatomical and $^{19}\text{F}$ -MRI setup

Given the lacking  $^1\text{H}$  channel, an imaging setup including 3D-printed components was devised to acquire colocalized anatomical and  $^{19}\text{F}$ -CRP images.

### 2.2.1 | Animal bed modification

The standard animal bed uses a lever that elevates the bed, lifting the mouse head closer to the  $^{19}\text{F}$ -CRP. This feature hampers position reproducibility. To ensure spatial alignment of both  $^{19}\text{F}$ -CRP and anatomical images, a 3D-printed

blocking component (Y-axis blocker) was designed to eliminate movement in the Y-axis (Figure 1A). Additionally, a new head holder was designed and 3D-printed to place the mouse head closer to the CRP surface (Figure 1A).

### 2.2.2 | $^1\text{H}$ -MRI setup

The 72-mm-volume resonator was positioned around the center tube holding the  $^{19}\text{F}$ -CRP. Anatomical images were acquired after a CRP replica (dummy), inserted from the back of the scanner, was kept in place while the animal bed was inserted from the front.

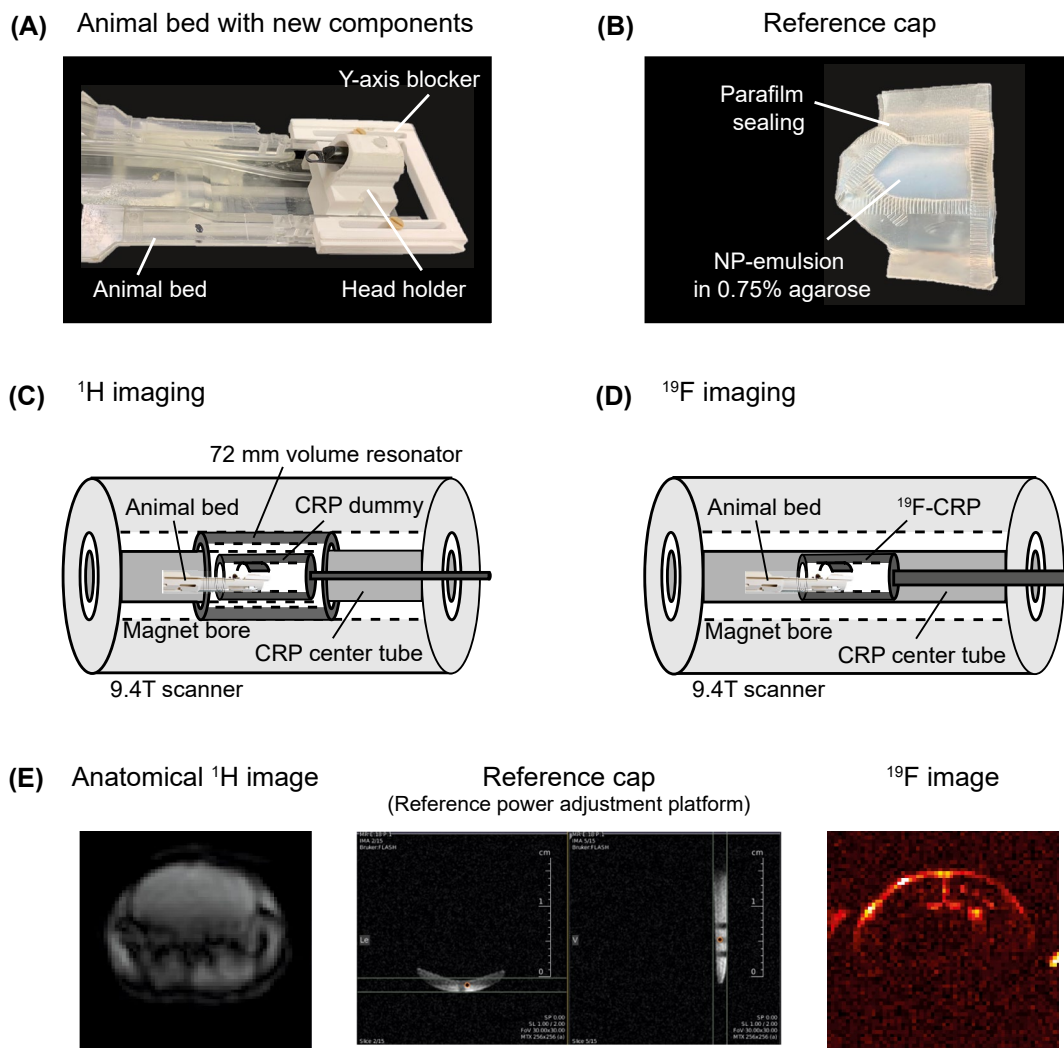


**FIGURE 1** Anatomical and fluorine-19 ( $^{19}\text{F}$ ) imaging setup designed for a single-tuned cooled transceive surface RF probe (CRP). (A) Close-up view of the animal bed provided by the vendor with a custom-designed component that eliminates mobility in the y-axis (y-axis blocker) and a new head holder to bring the animal's head closer to the surface of the CRP. (B) Reference cap containing  $^{19}\text{F}$ -loaded nanoparticles (NPs) to perform  $^{19}\text{F}$ -CRP reference power adjustments and as reference for quantification. (C,D)  $^1\text{H}/^{19}\text{F}$  imaging setups. (E) For exemplary in vivo images, anatomical images and slice planning are performed using a 72-mm volume resonator and a CRP dummy. Afterward, reference power calibrations are carried out using the reference cap, and  $^{19}\text{F}$  images are acquired using the  $^{19}\text{F}$ -CRP

### 2.2.3 | $^{19}\text{F}$ -MRI setup

Both animal bed and dummy were removed and the  $^1\text{H}$ -volume resonator was retracted toward the back of the scanner. The  $^{19}\text{F}$ -CRP was mounted as instructed by the vendor.

A  $^{19}\text{F}$ -NP reference cap (section 2.3) was placed over the mouse head to perform  $^{19}\text{F}$ -CRP reference power adjustments and to acquire images for quantification (Figure 1B). Afterward, it was removed to acquire in vivo  $^{19}\text{F}$  images (Figure 1C–E).

## 2.3 | Sample and animal preparation

Table 1 summarizes all MR measurements, RF coils, and samples used.

Perfluoro-15-crown-5-ether (1200 mM PFCE; Fluorochem, Hadfield, United Kingdom;  $f \approx 376.629$  MHz) nanoparticles were prepared as described.<sup>27,28</sup>

To characterize  $^{19}\text{F}$ -CRP  $B_1$  fields,  $B_1$  maps and RARE images were used as follows:

- Low- $T_1$  uniform phantom: 15-mL tube (ID = 14.6 mm, length = 120 mm, wall thickness = 0.8 mm; Fischer Scientific, Waltham, MA, USA) with 33.3% 2,2,2-trifluoroethanol (Carl Roth & Co., Karlsruhe, Germany;  $f \approx 376.633$  MHz) in water with 0.08 mM of gadolinium (Magnevist 0.5 mmol/ml; BayerVital, Leverkusen, Germany) yielding  $T_1 \approx 300$  ms.
- High- $^{19}\text{F}$  concentration reference cap (Figure 1B): homogeneous mixture of 60 mM NPs in 1 mL 0.75% agarose (dimensions  $20 \times 15$  mm<sup>2</sup>; thickness  $\approx 1.5$  mm) sealed within PARAFILM (thickness = 0.14 mm; Sigma-Aldrich, St. Louis, MO, USA).

Both sets of maps were acquired separately to consider tube thickness (0.8 mm). This accounts for more than half the number of pixels of the reference cap.

Phantoms and mice were used to evaluate the performance of the  $B_1$  correction methods as follows:

- Test uniform phantom: 15-mL tube containing 0.2 mM of 2,2,2-trifluoroethanol in water. To achieve  $T_1 \approx 1870$  ms (in vivo PFCE-NPs  $T_1$ ; see section 3), 0.006 mM gadolinium was used.
- In vivo and ex vivo mice: EAE was induced in female SJL/J mice as described.<sup>26</sup> Animals were weighed and scored (0–5) daily for disease signs. Intravenous injections of  $^{19}\text{F}$ -NPs (10  $\mu\text{mol}$  PFCE in 200  $\mu\text{L}$ ) were administered daily from day 5 following EAE induction until the experiment end. Respiration and temperature

were monitored during measurements. All animal experiments were approved by the Animal Welfare Department of the LAGeSo in Berlin and in accordance with international guidelines (86/609/EEC).

In vivo  $^{19}\text{F}$ -NPs  $T_1$  for *model-based corrections* was calculated in  $n = 3$  EAE mice using a combination of ketamine-xylazine (initial dose 400  $\mu\text{L}$ , followed by 100–200  $\mu\text{L}$  injections administered intraperitoneally every 45 minutes until the end of the MR examination) to avoid confounding  $^{19}\text{F}$  signal. Ex vivo  $T_1$  of PFCE-NPs was computed on  $n = 3$  ex vivo phantoms prepared as described subsequently.

In vivo  $^1\text{H}$  and  $^{19}\text{F}$  images were acquired on another  $n = 3$  EAE mice from which  $n = 2$  animals are shown. These were anesthetized with isoflurane (2% initial dose, 0.5%–1% maintenance).  $^1\text{H}$ - and  $^{19}\text{F}$ -MRI of an ex vivo phantom containing the central nervous system (CNS) of a EAE mouse perfused/fixed as described<sup>8</sup> and embedded in a 15-mL tube filled with 4% paraformaldehyde (Santa Cruz Biotechnology, Dallas, TX, USA) were also performed.

- A reference cap (24 mM NP emulsion) was prepared as described previously for  $^{19}\text{F}$ -CRP adjustments and signal quantification of in vivo and ex vivo mice. A similar construction of smaller dimensions ( $10 \times 5$ ) mm<sup>3</sup> was prepared to fit within the volume resonator.

## 2.4 | Magnetic resonance experiments

$^{19}\text{F}$ -CRP reference power calibrations were performed on a 1-mm slice parallel and close to the probe surface. All images were acquired as repetitions in axial and sagittal orientation. Noise scans (number of excitations [NEX] = 1 and reference power = 0 W) were acquired after each RARE image for SNR map computation.

### 2.4.1 | $^{19}\text{F}$ -CRP $B_1$ field characterization

The  $B_1$  fields of the  $^{19}\text{F}$ -CRP were characterized.<sup>23</sup> Separate sets of maps were determined using the low- $T_1$  uniform phantom and the high- $^{19}\text{F}$  concentration reference cap as follows:

- Flip angle (FA) mapping: FLASH measurements with TE/TR = 2.16/3000 ms, FOV = (25  $\times$  25) mm<sup>2</sup>, matrix = 96  $\times$  96, 5 slices (gap/thickness = 0.5/2 mm), 1 hour per orientation; FA = 60°/120°/240° (uniform phantom) and FA = 60°/120° (reference cap).
- $B_1$  mapping: FLASH measurements with parameters as described previously and FA = 5° in both cases.

TABLE 1 Detailed overview of measurements, RF coils, and samples used

Purpose	MR protocol	RF coil	Nucleus	Sample(s)	Acquisition time <sup>a</sup>
Acquired images ( <sup>19</sup> F-CRP, anatomical, and references):					
Test images and corresponding anatomical images	FLASH	72-mm linear volume resonator	<sup>1</sup> H	Ex vivo mouse phantom	30 minutes per orientation
	RARE	CRP	<sup>19</sup> F	In vivo mice	15 minutes per orientation
	RARE	CRP	<sup>19</sup> F	24-mM ref. cap (ex vivo, in vivo)	15 minutes per orientation
				Test uniform phantom	3 seconds
				Ex vivo phantom	6 hours per orientation
				In vivo mice	45 minutes per orientation
Reference images for comparison and corresponding anatomical images	FLASH	<sup>1</sup> H/ <sup>19</sup> F volume resonator	<sup>1</sup> H	Ex vivo mouse phantom	30 minutes per orientation
	RARE	<sup>1</sup> H/ <sup>19</sup> F volume resonator	<sup>19</sup> F	24-mM ref. cap (ex vivo only)	30 minutes per orientation
	RARE	<sup>1</sup> H/ <sup>19</sup> F volume resonator	<sup>19</sup> F	Test uniform phantom	1 hour
				Ex vivo phantom	6 hours per orientation
T <sub>1</sub> mapping for uniform phantom	RARE with variable TR	<sup>1</sup> H/ <sup>19</sup> F volume resonator	<sup>19</sup> F	Test uniform phantom	24 minutes
T <sub>1</sub> values of PFCE-loaded NPs	Non-localized MRS	<sup>1</sup> H/ <sup>19</sup> F volume resonator	<sup>19</sup> F	24-mM and 60-mM ref. caps	35 minutes
	PRESS	<sup>1</sup> H/ <sup>19</sup> F volume resonator	<sup>19</sup> F	Ex vivo phantoms (n = 3)	30 minutes
				In vivo mice (n = 3)	1 hour 8 minutes
<b>Sensitivity correction:</b>					
Uniform phantom images	RARE	CRP	<sup>19</sup> F	Low-T <sub>1</sub> uniform phantom	1 hour per orientation
<b>Model-based correction:</b>					
FA and B <sub>1</sub> mapping	FLASH	CRP	<sup>19</sup> F	Low-T <sub>1</sub> uniform phantom	1 hour per FA and orientation
	FLASH	CRP	<sup>19</sup> F	Highly fluorinated ref. cap	1 hour per FA and orientation

Abbreviation: CRP, cryogenically-cooled transceive surface RF probe; FA, flip angle; NPs, nanoparticles. ref., reference.

<sup>a</sup>Indicative values: Scan times may vary when using different scan parameters (e.g., spatial resolution, echo train length, TR).

For the *sensitivity correction method*, RARE images of the low- $T_1$  uniform phantom were acquired ( $TE/TR = 4.62/1000$  ms, same geometry, echo train length (ETL) = 32, bandwidth = 50 kHz, centric encoding with flipback, 1 hour per orientation). All  $^{19}\text{F}$ -RARE images were measured using these scan parameters with varying acquisition times.

#### 2.4.2 | $T_1$ relaxation times (reference, ex vivo, in vivo) of PFCE-NPs

Due to the inherent  $^{19}\text{F}$  characteristics (low SNR, signal sparsity, lack of an a priori known location), determining in vivo  $T_1$  with  $T_1$  mapping was unfeasible. We applied MRS techniques using the  $^1\text{H}/^{19}\text{F}$  volume resonator as follows:

- Non-localized spectroscopy (block pulse, 10 TRs [250–10 000 ms], number of acquisitions [NA] = 64, acquisition time [TA] = 35 minutes) to compute  $T_1$  values of the two reference caps (24 mM, 60 mM).
- Localized spectroscopy (PRESS) to compute  $T_1$  values in the brain after  $^{19}\text{F}$ -NP administration in ex vivo phantoms ( $n = 3$ , 12 TRs [250–15 000 ms], NA = 64, TA = 32 minutes) and in vivo mice ( $n = 3$ , 8 TRs [412.5–13 000 ms], NA = 128, TA = 1 hour 8 minutes). A default  $B_0$  field map was measured before each experiment to optimize shim adjustment (MAPSHIM) computed on  $^1\text{H}$  using a 3D cuboid shape fitting the mouse brain.

#### 2.4.3 | Uniform phantom MR measurements

A  $^{19}\text{F}$ -MR image of the test uniform phantom was acquired with the  $^{19}\text{F}$ -CRP (RARE: same parameters, 3 seconds, axial orientation) to assess  $B_1$  correction performance in low SNR scenarios far from the probe surface. A reference  $^{19}\text{F}$  image (RARE: same parameters, 1 hour) and a  $T_1$  map (RARE with variable TR [250–10 000 ms], ETL = 2, linear phase encoding, other parameters same as RARE scan, 24 minutes) were acquired with the  $^1\text{H}/^{19}\text{F}$  volume resonator for comparison.

#### 2.4.4 | Ex vivo and in vivo MR measurements

Slice planning and anatomical images (FLASH:  $TE/TR = 3/120$  ms, same FOV, matrix =  $256 \times 256$ , TA = 30/15 minutes per orientation ex vivo and in vivo, respectively) were acquired with the 72-mm volume resonator.

$^{19}\text{F}$ -MR images were measured with the  $^{19}\text{F}$ -CRP with (RARE: same parameters, 15 minutes per orientation both ex vivo and in vivo) and without (RARE: same parameters,

6 hours/45 minutes per orientation ex vivo and in vivo, respectively) reference cap.

Reference images were acquired with the  $^1\text{H}/^{19}\text{F}$  volume resonator in ex vivo phantoms: reference cap ( $^{19}\text{F}$  RARE: same parameters, 30 minutes per orientation) and phantoms ( $^{19}\text{F}$  RARE: same parameters, 6 hours per orientation;  $^1\text{H}$  FLASH: same parameters, 1 hour per orientation).

### 2.5 | Data analysis

Data analysis was performed using *MATLAB* (The MathWorks, Natick, MA, USA).

#### 2.5.1 | MRI data preprocessing

All data followed the same pre-processing workflow:

1. Complex averaging over smaller subsets of the total number of repetitions to mimic different scan times followed by a sum-of-squares (SoS) combination of the two channels ( $^{19}\text{F}$ -CRP):
  - Uniform phantom: one subset of a 3-second acquisition.
  - Ex vivo phantoms: four subsets corresponding to 15-minute and 1-3-6-hour acquisitions. Same with  $^1\text{H}/^{19}\text{F}$  volume resonator for comparison.
  - In vivo mice: three subsets corresponding to 15-30-45 minutes.
  - Reference caps: one subset corresponding to the total scan time.
2. Noise bias correction:<sup>29</sup>
  - $^{19}\text{F}$ -CRP: noncentral  $\chi$  distribution<sup>23</sup> using a lookup table for  $n = 2$  channels.<sup>30</sup>
  - Volume resonator: Rician distribution<sup>23</sup> using a lookup table for  $n = 1$  channels.<sup>30</sup>
3. Thresholding (SNR cutoff = 3.5) and removal of isolated groups of < 3 connected pixels.

#### 2.5.2 | $^{19}\text{F}$ -CRP $B_1$ field characterization and RARE SI model computation

The  $B_1$  maps were computed and denoised as detailed<sup>23</sup> (10<sup>th</sup>-order and 8<sup>th</sup>-order polynomials for the low- $T_1$  uniform phantom and the high- $^{19}\text{F}$  concentration reference cap, respectively).

The RARE SI model was calculated as a function of FA and  $T_1$  relaxation value ( $SI = f(FA, T_1)$ ) using extended phase graphs<sup>31–33</sup> (EPGs). This algorithm provides a tool that depicts the magnetization response and allows computing echo intensities in multi-pulse MR sequences.

RARE scans with the same MR parameters as above were simulated for 20 equispaced  $T_1$  values (150–2050 ms) and 32 excitation FAs ( $5^\circ$ – $160^\circ$  in  $5^\circ$  steps). Finally, an 8<sup>th</sup>-degree polynomial was fitted<sup>23</sup> to the simulated data for faster computation of results for arbitrary FAs and  $T_1$  values, which did not introduce any oscillations or error within the desired parameter space ( $R^2 = 1.0$ , root-mean-square-error (RMSE) =  $5.5 \times 10^{-4}$ ).

### 2.5.3 | $T_1$ relaxation times (reference, ex vivo, in vivo) of PFCE-NPs

PFCE-NPs typically show a single peak at  $f \approx 376.629$  MHz. A Lorentzian line-broadening (factor = 70) and automatic phase correction (TopSpin 2.1) were applied. To compute  $T_1$  values from MRS data, peak values were fitted as SI vs. TR datapoints on an exponential growth. Mean values and SDs were computed.  $T_1$  values were used to correct  $B_1^+$  using the *model-based method*.

### 2.5.4 | $B_1$ correction methods

The  $B_1$  of  $^{19}\text{F}$ -CRP images was corrected using the *sensitivity* (uniform phantom) and *model-based* (reference caps, phantoms, and in vivo mice) methods.<sup>23</sup> All post-processing was performed using software openly available on Github (pramosdelgado/B1correction-toolkit).

### 2.5.5 | $^{19}\text{F}$ signal quantification

The 24-mM reference cap was used as reference to determine absolute  $^{19}\text{F}$  concentrations as follows:

$$c_{\text{sample}} = \frac{\overline{SI}_{\text{sample}} \times c_{\text{ref}}}{\overline{SI}_{\text{ref}}} \quad (1)$$

where  $\overline{SI}_{\text{sample}}$  and  $SI_{\text{ref}}$  are the SIs for the sample and the reference, respectively, and  $c_{\text{sample}}$  and  $c_{\text{ref}}$  are the corresponding concentrations. To compute  $SI_{\text{ref}}$ , a square-shaped region of interest (ROI;  $3 \times 3$  pixels) was selected in a  $B_1$ -corrected homogeneous region, in the center of the reference cap.

## 2.6 | Monte Carlo SNR simulations to estimate the $^{19}\text{F}$ concentration uncertainty

Given the sparse nature of  $^{19}\text{F}$  images and the spatially varying  $B_1$  fields of the  $^{19}\text{F}$ -CRP, we computed concentration uncertainty maps after  $B_1$  correction as follows (Figure 2):

**Step 1.** Monte Carlo SNR simulations<sup>34,35</sup> (1000 iterations) were performed using measured ( $T_1$  values) and synthetic data (SI computed using the simulated RARE SI model). Simulation parameters (Table 2) were defined to mimic realistic excitation FAs,  $B_1^-$ -values, and SNRs within the sample. Shorter parameter ranges were chosen for the reference cap after inspection of the central region of the FA,  $B_1^-$ , and SNR maps obtained (section 2.5.5). This was crucial to reduce matrix size and avoid memory problems.

**Step 2.** Noise levels for the prescribed SNR values were fixed for a  $90^\circ$  excitation and  $B_1^- = 1$  using a “reverse model-based correction” (inverse steps of the *model-based correction*<sup>23</sup>).

**Step 3.** For each combination of reference and sample FA,  $B_1^-$  and  $T_1$  values, the CRP SI (for reference and sample) was calculated and separated into two channels. For each Monte Carlo iteration, complex Gaussian noise was added to both channels, and a SoS reconstruction was computed to simulate a noncentral  $\chi$  distribution. A noise bias correction was performed as described, followed by a *model-based correction*. Finally, the concentration was estimated using equation (1). The mean SNR and mean and SD of the corrected SI throughout the 1000 iterations were determined for both reference and sample, along with the mean and SD of the concentration. Since the Monte Carlo samples conformed to a Gaussian distribution of mean  $\approx 1$  (section 3), the corresponding uncertainties in corrected SI and concentration were defined as  $\text{SD} \times 100$  (%).

**Step 4.** To compute the uncertainty map of an acquired  $^{19}\text{F}$  image, measured data (FA,  $B_1^-$ , and SNR maps,  $T_1$  value) were fed to the corresponding Monte Carlo uncertainty model. The uncertainties were interpolated pixel-wise using a simple linear regression after logarithmically transforming the SNR and uncertainty data and eliminating SNR values  $< 1$ .

## 2.7 | Correction method evaluation and validation

$B_1$  correction methods were validated using the following methods on the uniform phantom:

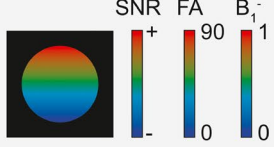
### 2.7.1 | Central profile plots of uniform phantoms

We quantified the improvement in image homogeneity by plotting normalized vertical SI profiles of original, corrected, and reference images against the distance from the CRP surface.

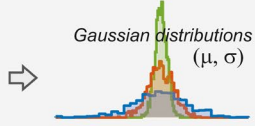
## Parameter definition

- STEP 1**
- Number of Monte Carlo iterations
  - Ground truth values for SI and concentration (sample, ref.)
  - Sample: excitation FA, normalized  $B_1^-$ ,  $T_1$  relaxation times (ex vivo, in vivo) and SNR
  - Reference cap: excitation FA, normalized  $B_1^-$ ,  $T_1$  relaxation times (in agarose) and SNR
  - Lookup table for bias correction
  - RARE SI model

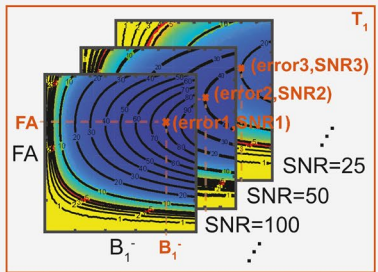
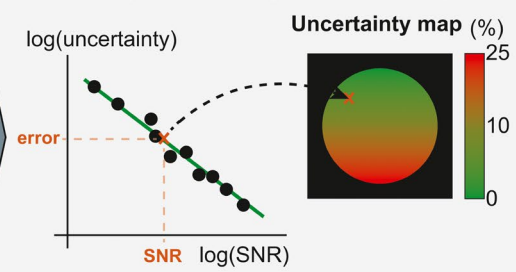
## Compute fixed noise levels

- STEP 2**
1. "Reverse" model-based correction to compute  $SI_{CRP}$ :
    - Sample: FA = 90°,  $B_1^- = 1$ ,  $T_1 = 1869$  ms
    - Ref.: FA = 90°,  $B_1^- = 1$ ,  $T_1 = 936$  ms
  2. Calculate noiseSigma for defined SNR values
- 

## SNR simulations

- STEP 3**
- For each FA,  $B_1^-$  and  $T_1$  relaxation time of ref. and sample:
    1. Compute pixel CRP SI ("reverse model-based correction")
    2. Separate in 2 channels
  - For each Monte Carlo iteration:
    1. Add complex Gaussian noise and perform SoS reconstruction
    2. Perform noise bias correction
    3. Model-based  $B_1$  correction
    4. Determine concentration:  $c_{sample} = \frac{SI_{sample} \times c_{ref}}{SI_{ref}}$   $c$  = concentration  
 $SI$  = signal intensity
  - 3. Compute statistics:
    - Mean SNR
    - Mean and SD of corrected SI
    - Mean and SD of concentration (signal quantification)
- 

## Uncertainty map estimation

- STEP 4**
- Error dataset for desired (FA,  $B_1^-$ ,  $T_1$ )
- 
- Linear fit in log-log plot and uncertainty map calculation (find uncertainty for desired SNR)
- 

**FIGURE 2** Monte Carlo SNR simulation and uncertainty map estimation workflow using measured and synthetic data. After determining the noise levels for the defined SNR values, Monte Carlo simulations are performed for each flip angle (FA),  $B_1^-$ , and  $T_1$  relaxation time of the sample and reference by adding noise, computing a noise bias correction, and calculating a model-based  $B_1$  correction. Concentration was also estimated. Statistics including mean SNR, mean and SD of corrected signal intensity (SI), and mean and SD of the concentration were computed after each run. These simulations are then used to derive uncertainty maps for the measured data using the FA,  $B_1^-$ ,  $T_1$ , and SNR measured at each pixel using a linear regression in a log-log plot (error vs. SNR). Abbreviations: Ref., reference; SoS, sum-of-squares

TABLE 2 Summary of simulation parameters for Monte Carlo SNR simulations

Parameters	Initialization values	Ranges and steps	Number of elements
<b>Ground-truth data</b>			
Ground-truth SI sample	1	–	1
Ground-truth SI reference cap	1	–	1
Ground-truth concentration reference cap	1	–	1
<b>Sample data</b>			
Excitation FA (relative to 90°)	5°–130°	1° steps	126
Normalized B <sub>1</sub> <sup>-</sup>	0–1	0.01 steps	101
SNR values (fixed at 90° excitation)	0–1500	0–10 in 0.5 steps 11–25 in 1.0 steps 27.5–100 in 2.5 steps 105–500 in 5 steps 510–1500 in 10 steps	246
T <sub>1</sub> values	936 ms, 818 ms, 1869 ms	–	3
<b>Reference cap data</b>			
Excitation FA (relative to 90°)	50°–60°	5° steps	3
Normalized B <sub>1</sub> <sup>-</sup>	0.8–0.7	0.05-steps	3
SNR value (fixed at 90° excitation)	500	–	1
T <sub>1</sub> values	936 ms	–	1

## 2.7.2 | Image homogeneity assessment

The percentage of integral uniformity (PIU)<sup>36</sup> was computed for three internally tangential circular ROIs with increasing diameter placed on the central vertical line filling the region with signal.

## 2.7.3 | Quantification performance

Ten ROIs were placed at pseudo-randomized positions (Figure 5B) on original, corrected, and reference images. Mean absolute percentage errors (MAPEs) were computed relative to the reference (volume resonator) images, as follows:

$$MAPE = \frac{|\overline{SI}_{reference} - \overline{SI}_{corrected}|}{\overline{SI}_{reference}} \times 100 (\%)$$

where  $\overline{SI}_{reference}$  and  $\overline{SI}_{corrected}$  are the mean SI in reference and corrected images.

A value was calculated for the original image and the three corrections summing over an increasing number of ROIs (top to bottom), with increasing distances from the CRP surface and decreasing SNR. Corrections were classified as excellent (MAPE ≤ 10%, green), good

(10% < MAPE ≤ 25%, orange), or unacceptable (MAPE > 25%, red).

## 2.7.4 | Statistics

Normality was assessed using the D'Agostino-Pearson test. Because none of the MAPEs on original or corrected data conformed to a Gaussian distribution, a Friedman non-parametric one-way repeated-measures ANOVA test was used followed by Dunn's post-hoc test, in which all corrections were compared to original data (*p*-values < 0.001 were considered significant). The statistical analysis was performed using *GraphPad Prism 5* (GraphPad Software, La Jolla, CA, USA).

## 3 | RESULTS

### 3.1 | <sup>19</sup>F-CRP B<sub>1</sub>-field characterization and RARE SI model

The sensitivity maps (Figure 3A,D) and the FA maps (relative to an excitation FA = 90°, Figure 3B,E) of the <sup>19</sup>F-CRP revealed a strong decline with increasing distance from the RF probe surface, in both axial and sagittal orientations.

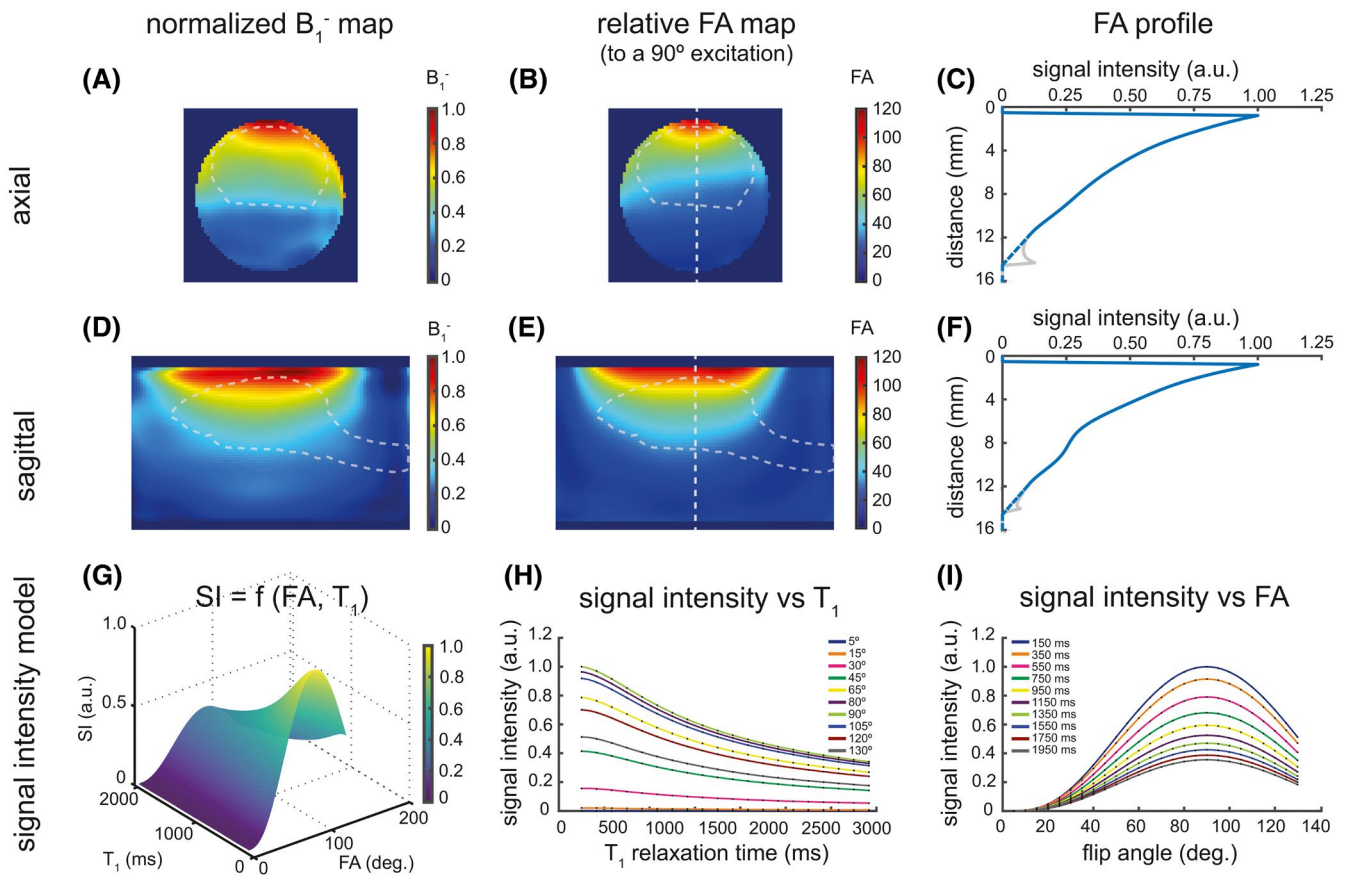


**FIGURE 3**  $B_1$  field maps of the quadrature  $^{19}\text{F}$  cryogenically-cooled transceive surface RF probe ( $^{19}\text{F}$ -CRP) and SI model used. (A–E)  $B_1^-$  and relative FA maps to a  $90^\circ$  excitation FA in axial (A,B) and sagittal (D,E) orientation. The expected position of the mouse brain relative to the  $^{19}\text{F}$ -CRP is outlined as a dashed gray line. (C,F) Corresponding normalized central vertical profiles. The gray line depicts the artifact miscalculated by the polynomial fit at low-SNR regions far away from the RF probe surface. The physically correct value is depicted using blue dotted lines. The simulated 3D SI model (G) shows the dependency of the rapid acquisition with refocused echoes (RARE) SI on the  $T_1$  relaxation time and FA. H,I, The 2D-projections of SI vs.  $T_1$  and SI vs. FA, respectively

The  $B_1^+$  inhomogeneity is clearly depicted in Figure 3C (axial) and Figure 3F (sagittal), which show the normalized central vertical profile lines. The maximum distance until which there is signal above the detection threshold ( $\text{SNR} > 3.5$ ) is, in this case, approximately 14.6 mm from the CRP surface.

Figure 3G shows the 3D view of the RARE SI model simulated using EPG simulations. The SI was modeled as a function of FA and  $T_1$ . The SI demonstrates a lower SI with increasing  $T_1$  (Figure 3H) and maximal SI for FA =  $90^\circ$  (Figure 3I). When using EPG simulations, the *hybrid* and *sensitivity methods* yielded the same results up to a constant factor (Supporting Information). Therefore, we only used the *sensitivity* and *model-based correction* moving forward.

### 3.2 | $T_1$ relaxation times (reference, ex vivo, in vivo) of PFCE-loaded NPs

Calculated  $T_1$  values for PFCE-NPs in agarose (reference caps,  $935.9 \pm 10.0$  ms) using non-localized MRS agreed

with previously published values at 9.4 T.<sup>37,38</sup>  $T_1$  values of  $^{19}\text{F}$ -NPs in inflammatory lesions in the brain (PRESS) were  $818.1 \pm 13.4$  ms (ex vivo) and  $1868.7 \pm 43.9$  ms (in vivo). This indicated an effective reduction of 117.8 ms in  $T_1$  for ex vivo compared to the reference caps, and an increase of nearly 1 second in  $T_1$  in vivo measurements. Exemplary spectra are shown in Supporting Information Figure S1.

### 3.3 | Monte Carlo SNR simulations to estimate the $^{19}\text{F}$ concentration uncertainty

Figure 4A–C shows the concentration uncertainty (uncertainty =  $\text{SD} \times 100$  [%]) for all FAs/ $B_1^-$  and three SNR values fixed for FA =  $90^\circ$ ,  $B_1^- = 1$ , and  $T_1 = 1869$  ms (in vivo). For the reference, representative values (FA =  $60^\circ$ ,  $B_1^- = 0.8$ ) were used. The level of uncertainty increases with decreasing FAs and  $B_1^-$ . This trend is more pronounced for regions farther away from the RF probe surface. The contour lines represent SNR values. The green and red

isolines depict the border of the regions where uncertainty  $\leq 10\%$  and  $\leq 25\%$ , respectively. These borders occur at  $\text{SNR} \approx 10.1$  and  $\text{SNR} \approx 4.25$ , respectively, independent of the  $\text{FA}/B_1^-$  and  $\text{SNR}$  combination.

We studied the linear dependence of the SD of both corrected SI and concentration on  $\text{SNR}$  for exemplary data ( $\text{FA} = 90^\circ$ ,  $B_1^- = 1.0$ , in vivo  $T_1$ ) using the *model-based method* (Figure 4D, linear fit, dashed orange line). The corrected SI of the sample (blue dots) demonstrated a linear trend throughout the  $\text{SNR}$  range. The concentration SD (green boxes) was linearly dependent on the sample  $\text{SNR}$  until an  $\text{SNR} \approx 160$  ( $\text{SD} = 7 \times 10^{-3}$ ), after which it asymptotically approached a constant value of approximately  $3.5 \times 10^{-3}$  (uncertainty = 0.35%) due to small but non-negligible errors in the  $B_1^-$ -corrected data.

Finally, Figure 4E shows histograms and error bars<sup>39</sup> of the concentration calculated over the 1000 iterations corresponding to the three depicted example points ( $\text{FA} = 70^\circ$ ,  $B_1^- = 0.8/0.4/0.2$  as colored crosses on Figure 4C). The concentration samples exhibited a Gaussian shape with mean  $\approx 1$  ( $\mu_1 = 1.0003$ ,  $\mu_2 = 0.9964$ ,  $\mu_3 = 0.9834$ ) and increasing SD ( $\sigma_1 = 0.0564$ ,  $\sigma_2 = 0.1199$ ,  $\sigma_3 = 0.2529$ ) with decreasing  $\text{SNR}$ , as expected. This demonstrated that the model recovered SIs without introducing bias. Randomness was propagated such that the variability of the corrected SI (i.e., its SD) increased with decreasing  $\text{SNR}$ .

### 3.4 | Uniform phantom MR measurements

#### 3.4.1 | Corrected images

$B_1^-$  correction performance was assessed in a low- $\text{SNR}$  scenario at regions far from the probe surface using a low-concentration uniform phantom and a short acquisition. The  $\text{SNR}$  map is shown in Figure 5A. The original image shows a steep SI decay away from the RF probe surface, typical of transceive surface RF coils (Figure 5B). Compared with the reference image,  $B_1^-$ -corrected images (Figure 5C,D) yielded uniform SIs over the FOV (Figure 5E). A ghosting artifact due to fast RARE imaging is present in the uniform phantom image used for the *sensitivity method*, and in the test uniform phantom, producing an overshoot in the sensitivity-corrected image far from the probe surface.

#### 3.4.2 | Central profile plots

Corrected SI profiles demonstrated close correspondence with the reference RF coil (green area) up to a distance of approximately 6–7 mm from the CRP surface for our

specific scanning parameters, dimensions of the RF coil, and  $\text{SNR}$  (Figure 5F).

#### 3.4.3 | Image homogeneity assessment

The calculated PIU in the reference image was 91.4% within the largest ROI (distance from CRP surface = 7.8 mm), indicating no substantial inhomogeneities across the image. In contrast, a PIU of 13.6% was computed for the original image within the same ROI. Corrections yielded improved PIUs (56.7% for *model-based* and 32.4% for *sensitivity corrections*). In general, PIU degrades with increasing distance from the RF probe, where acquired image artifacts prevail (Figure 5H).

#### 3.4.4 | Quantification performance and statistics

According to our MAPE classification, only the *model-based correction* provided excellent results for  $\text{SNRs}$  between 38 and 7 (Figure 5G; ROIs = 1–7, distance = 2.1–6.3 mm). Uncorrected images showed high errors within this  $\text{SNR}$  range ( $84.7 \pm 85.8\%$ ). Within this region (distance = 2.1–6.3 mm), the *model-based correction* performed best ( $7.7 \pm 4.7\%$ ), followed by the *sensitivity correction*, which yielded good results ( $12.2 \pm 8.2\%$ ). Both corrections provided equally good results (*model-based*  $16.2 \pm 16.5\%$ , *sensitivity*  $19.7 \pm 16.6\%$ ) up to the eighth ROI (distance = 2.1–6.5 mm), in contrast to uncorrected images ( $89.9 \pm 95.6\%$ ). When considering all ROIs (distance = 2.1–7.6 mm), only the *model-based correction* ( $19.7 \pm 18.9\%$ ) yielded good results. In this case, the *sensitivity correction* provided unacceptable results ( $35.5 \pm 33.3\%$ ), but was still lower than the MAPE of uncorrected images ( $105.8 \pm 125.9\%$ ). Figure 5G also shows similarities between the proposed ranges using simulations (uncertainty  $\leq 10\%$  when  $\text{SNR} \geq 10.1$  and uncertainty  $\leq 25\%$  when  $\text{SNR} \geq 4.25$ ) and experimental results.

The *model-based correction* performed best overall, significantly reducing quantification errors compared with original mean errors (both  $B_1^-$  correction methods  $p < 0.001$ ; Figure 5I). Therefore, this method was used for further  $B_1^-$  corrections.

### 3.5 | Ex vivo MR measurements

Concentration maps of the ex vivo EAE phantom were computed for different measurement times (15 minutes [ $\text{NEX} = 300$ ], 1, 3, and 6 hours [ $\text{NEX} = 1200/3600/7200$ ]) using the 24-mM reference cap in images acquired with the reference

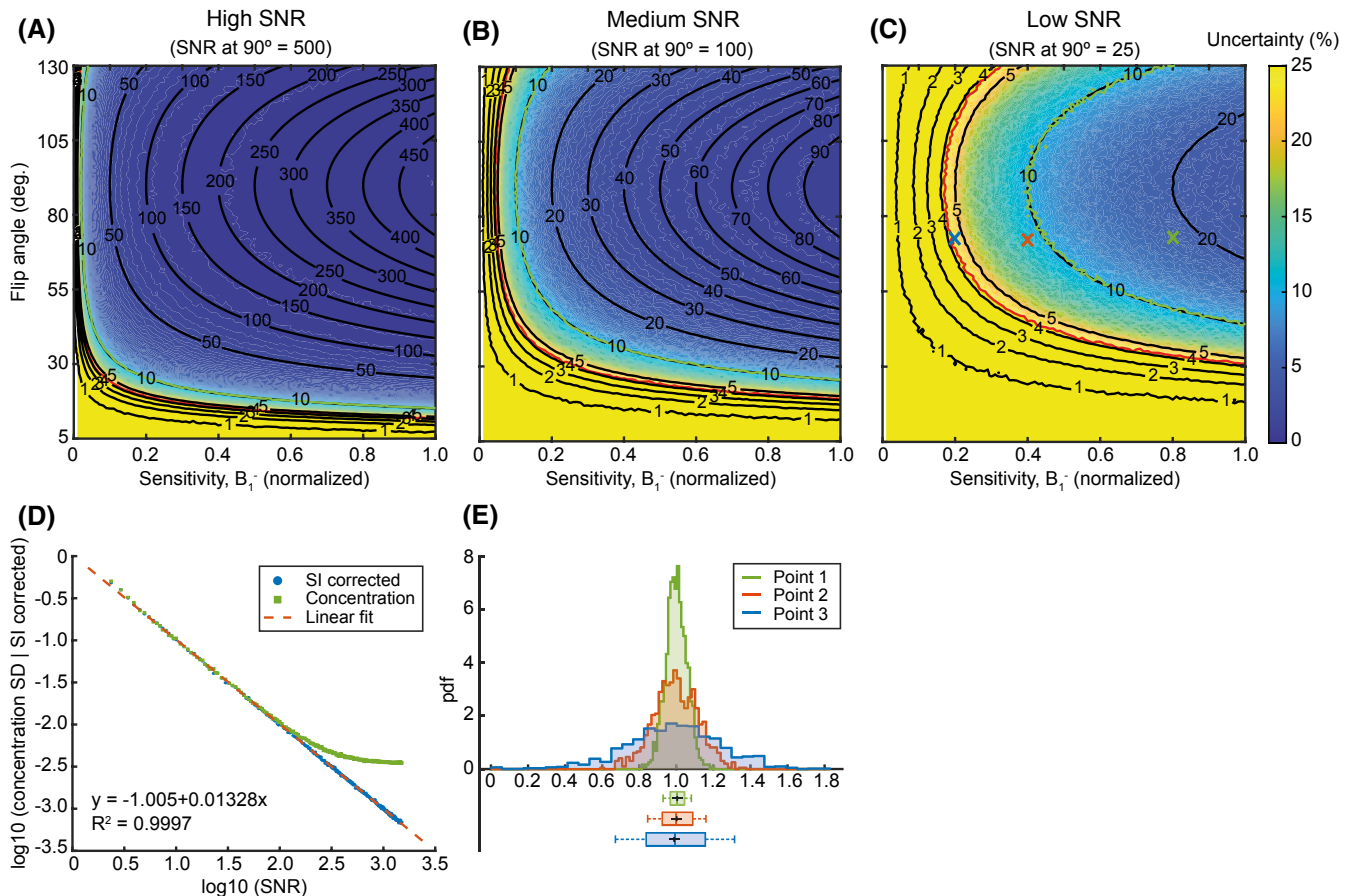


**FIGURE 4** The SNR simulation results corresponding to a *model-based correction* for  $T_1 = 1869$  ms (in vivo mouse) for SNR = 1000 (A), SNR = 500 (B), and SNR = 25 (C), fixed for a  $90^\circ$  excitation and  $B_1^- = 1$ . The contour lines represent equal SNR values (in black), and uncertainties of  $\leq 10\%$  (in green) and  $\leq 25\%$  (in red). (D) Linear dependence on the SD of the corrected SI and SNR, and quasi-linear dependence on the SD of the concentration and SNR (log-log plot). (E) Histogram from the Monte Carlo samples for the three points depicted in (C). In all three cases, the distributions exhibit a Gaussian distribution of mean  $\approx 1$  and increasing SDs (uncertainties) with decreasing SNR

volume resonator (Figure 6A) and original  $^{19}\text{F}$ -CRP images (Figure 6B). Qualitative comparison of the reference images after 3 hours and original CRP images after 15 minutes revealed distinct similarities, demonstrating the remarkable SNR capabilities of the CRP. However, the  $^{19}\text{F}$  signal at the lymph nodes, indicating accumulation of  $^{19}\text{F}$ -labeled inflammatory cells (white arrows) in reference images was absent in the  $^{19}\text{F}$ -CRP images, as the lymph nodes are located too far away from the CRP surface to be detected.

Assessment of the  $^{19}\text{F}$  concentration shown by original CRP images and corresponding *model-based  $B_1^-$ -corrected* images (Figure 6D) demonstrated that correction considerably improved the concentration estimation, compared with reference images (ground truth). The SNR maps from original CRP images showed the expected increase of SNR with scan time (Figure 6C), translating to fewer uncertainties in concentration (Figure 6E). Overall, the uncertainty maps indicated the reliability of the  $B_1^-$ -corrected concentration maps, with most

pixels being green (uncertainty  $\leq 10\%$ ) or orange ( $10\% <$  uncertainty  $\leq 25\%$ ). Images corresponding to the axial orientation are shown in Supporting Information Figure S2.

### 3.6 | In vivo MR measurements

We studied the performance of the *model-based correction* in a typically time-constrained and low-SNR in vivo EAE  $^{19}\text{F}$ -MRI experiment.

The first animal shown (Figure 7) exhibited severe clinical symptoms (score = 2.5), whereas the second (Figure 8) presented moderate clinical symptoms (score = 1.5). Images were acquired in axial and sagittal orientations for 15, 30, and 45 minutes (NEX = 300/600/900). Images corresponding to the axial orientation are shown in Supporting Information Figures S3 and S4.

Concentration maps of uncorrected images of mouse 1 (Figure 7A) showed an overestimation of  $^{19}\text{F}$

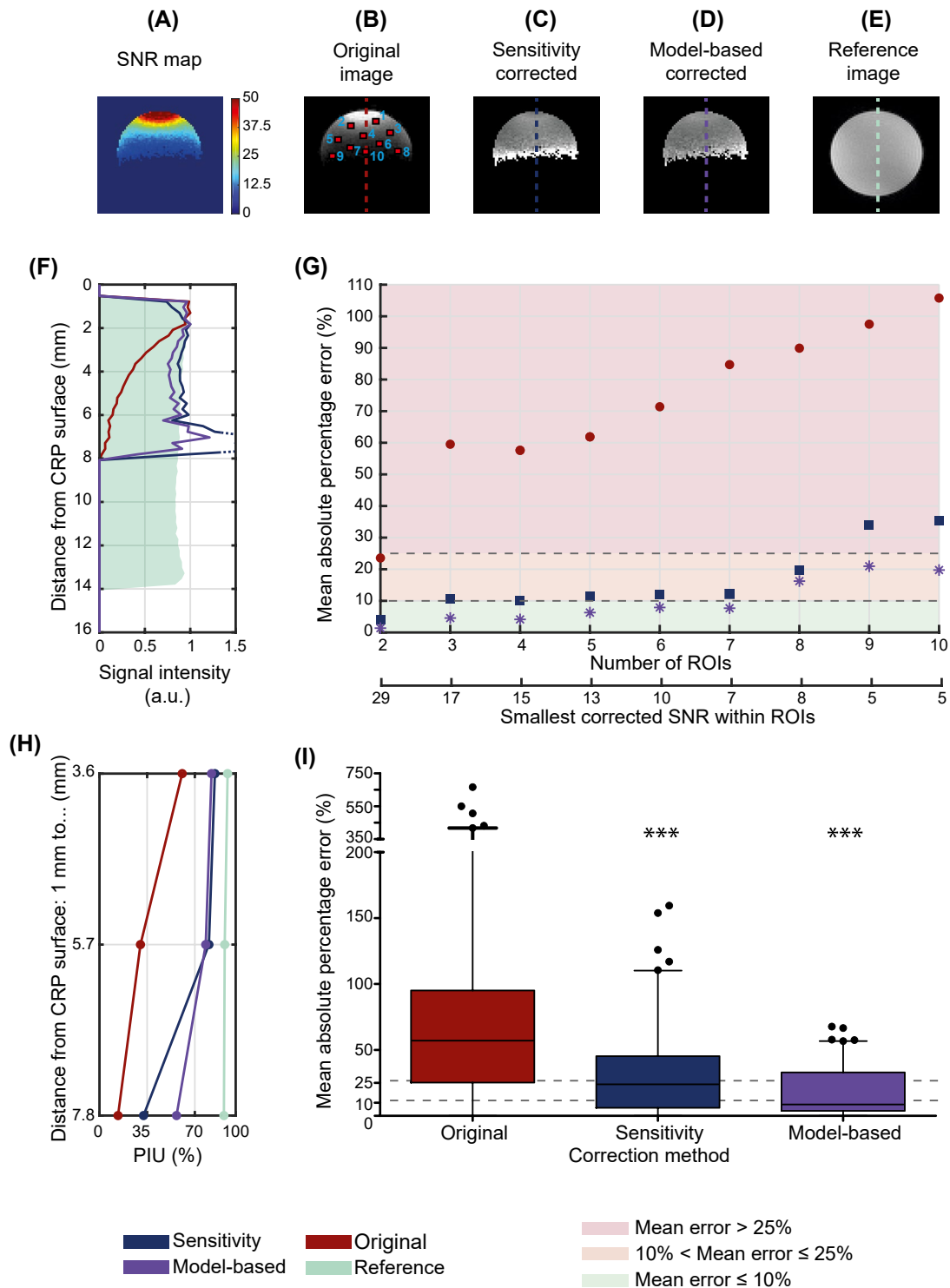


**FIGURE 5** Uniform phantom validation. (A) SNR map, (B) original (C,D) corrected, and (E) reference images, respectively. The original image includes the placement of the 10 regions of interest (ROIs) selected for error calculations. (F) Normalized SI profiles perpendicular to the RF coil surface. (G) Mean absolute percentage error (MAPE) of original and corrected images for an increasing number of ROIs demonstrates a remarkable reduction in errors after  $B_1$  correction compared to original images. The *model-based correction* provides quantitatively good results in regions far from the RF probe. (H) Percentage of integral uniformity (PIU) of corrected images shows a quantitative improvement in homogeneity in comparison with original images. (I) Statistical assessment of SI accuracy. Whiskers represent the 5th and 95th percentiles. Asterisks indicate statistical significance compared to uncorrected images

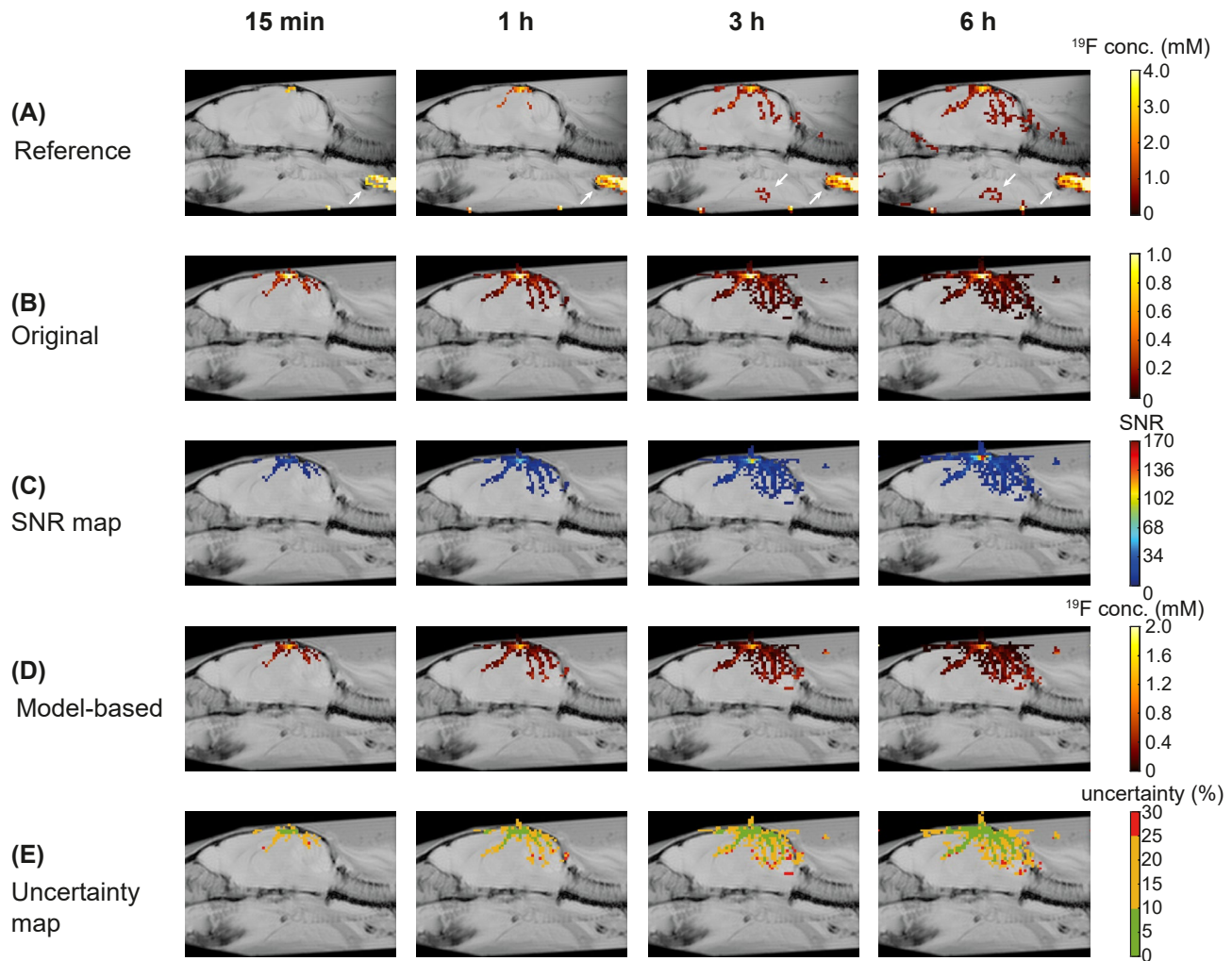


**FIGURE 6** Ex vivo phantom validation. Sagittal views of an ex vivo experimental autoimmune encephalomyelitis (EAE) mouse (score = 2.0) for increasing scan times (15 minutes, 1 hour, 3 hours, and 6 hours). Reference images (A) show impressive  $^{19}\text{F}$  signal in the lymph nodes, not visible with the  $^{19}\text{F}$ -CRP (B), since they are located too far away from the CRP surface to be detected. Distinct similarities when comparing CRP images after 15 minutes and those acquired with the volume resonator after 3 hours demonstrate the remarkable SNR capabilities of the CRP. (C) The SNR maps for the CRP images. (D) After performing the  $B_1$  correction, images show concentration values closer to the reference obtained with the volume resonator. (E) Uncertainty maps reveal the reliability of the  $B_1$ -corrected concentration maps, with most pixels indicating green (uncertainty  $\leq 10\%$ ) and orange ( $10\% < \text{uncertainty} \leq 25\%$ ) values

concentrations in regions close to the RF probe surface, which correspond to meningeal inflammatory cell infiltration, common in EAE. White arrows indicate external signals (i.e., in ears and other adjacent tissues), which are not corrected when located outside of the  $FA/B_1^-$  maps. The SNR maps (Figure 7B) correlate with the original concentration maps.

Following the *model-based  $B_1$  correction*, concentration maps (Figure 7C) showed reduced  $^{19}\text{F}$  concentration in regions close to the RF probe and increased  $^{19}\text{F}$  concentration in regions with high SNR far from the CRP surface. The reliability of the correction is represented by the concentration uncertainty maps that mostly show values with  $10 < \text{uncertainty} \leq 25\%$  (orange pixels) and  $\leq 10\%$  (green pixels) especially at higher SNR (Figure 7D).

Compared to mouse 1, mouse 2 presented with more  $^{19}\text{F}$  signal, even though its disease score was less severe. This is evident from the original concentration maps (Figure 8A) and corresponding SNR maps (Figure 8B). Mouse 2 exhibited meningeal inflammation, visible as a thin layer of  $^{19}\text{F}$  signal with an SNR ranging from 3.6 to 49.5 and  $^{19}\text{F}$  concentrations ranging from 0.1 to 1.7 mM, as well as inflammatory cell accumulation in deeper regions of the brain. After applying the *model-based correction* (Figure 8C), concentration maps showed an expected reduction in  $^{19}\text{F}$  concentration in the meninges and an increase in features far from the CRP surface. Corresponding concentration uncertainty maps (Figure 8D) demonstrate the reliability of the  $B_1$  corrections, with most pixels being orange ( $10\% < \text{uncertainty} \leq 25\%$ ) and green (uncertainty  $\leq 10\%$ ), especially at higher SNR.

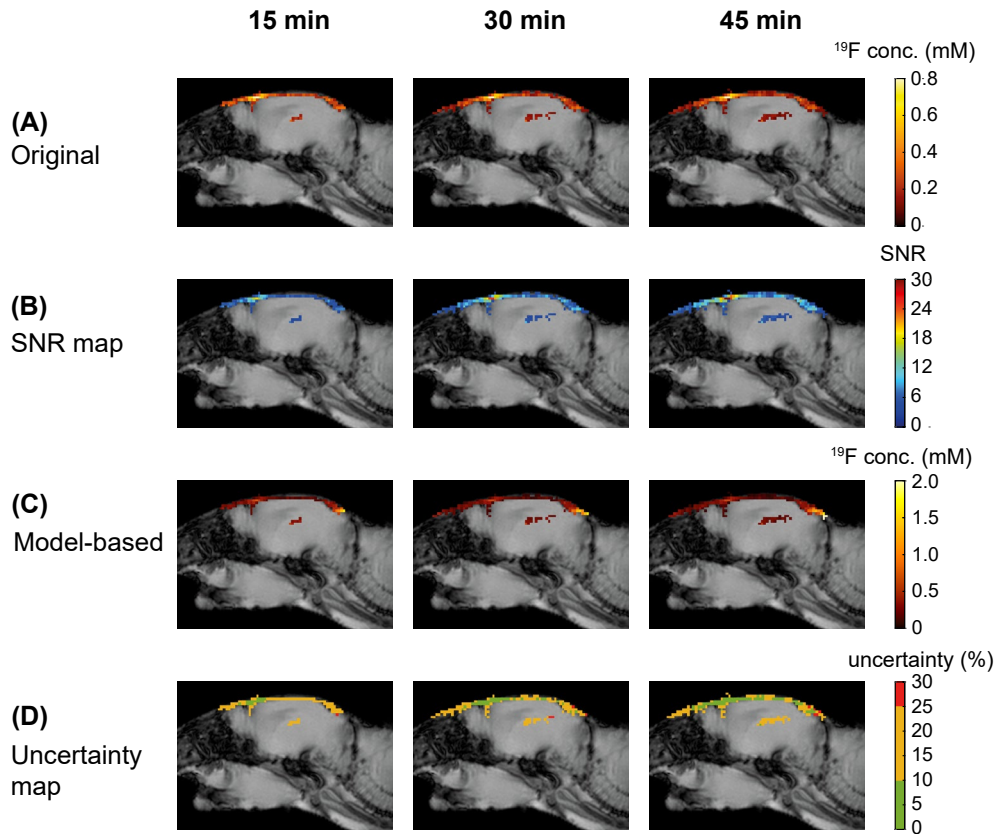


**FIGURE 7** In vivo EAE mouse 1 (score = 2.5) in sagittal orientation. Concentration maps of original images (A) show an initial overestimation of the  $^{19}\text{F}$  concentration in regions close to the RF probe surface (e.g., meninges), which partly correspond to regions with high SNR (B). (C)  $B_1$ -corrected images present an adjustment in scale, where  $^{19}\text{F}$  concentration not only depends on the distance to the CRP surface and SNR (heavily dependent on  $B_1^+$  and  $B_1^-$ ) but on the  $^{19}\text{F}$ -NPs accumulated per pixel. (D) The reliability of the  $B_1$ -corrected concentration maps is presented by the uncertainty maps, which show green (uncertainty  $\leq 10\%$ ) and orange ( $10\% < \text{uncertainty} \leq 25\%$ ) values for most pixels

## 4 | DISCUSSION

The potential of  $^{19}\text{F}$ -MR has long been recognized.<sup>1,40,41</sup> However, low in vivo  $^{19}\text{F}$  concentrations demand SNR-enhancing strategies. Transceive surface RF probes such as the  $^{19}\text{F}$ -CRP maximize SNR<sup>8</sup> but their inhomogeneous  $B_1$  field hampers quantification. To date, efforts in  $B_1$  field correction for  $^{19}\text{F}$ -MRI have been scarce, and usually limited to less complex imaging techniques.<sup>10,19,42,43</sup>

This study builds on our previous work on  $B_1$  correction methods tailored for  $^1\text{H}$  transceive surface RF probes and SNR-efficient RARE imaging,<sup>23</sup> to enable  $^{19}\text{F}$  signal quantification in low SNR time-constrained scenarios. Low-concentration uniform phantom images showed considerable increase in homogeneity after  $B_1$  correction even in low-SNR regions distal from the coil. Ex vivo concentration maps using reference caps demonstrated substantial improvement in concentration estimation, compared with reference images. We established a method to determine concentration error after  $B_1$  correction using Monte Carlo SNR simulations and an acquisition workflow to

co-localize  $^{19}\text{F}$ -CRP images with anatomical images from an external volume resonator. Furthermore, first in vivo  $^{19}\text{F}$ -nanoparticle  $T_1$  values were determined in EAE brains to compute *model-based corrections*. Successful implementation ultimately yielded the first quantitative in vivo  $^{19}\text{F}$ -MR images of inflamed EAE brains using a  $^{19}\text{F}$ -CRP.

Interestingly, differences in  $T_1$  were observed for PFCE-NPs in reference caps, ex vivo, and in vivo. This is in agreement with previous studies showing significant changes in  $T_1$  relaxation as a result of variations in temperature or chemical environment (e.g., pH, different tissue types).<sup>38,44</sup>

By introducing EPG simulations, here we reduced the burden of our previous strategy of preparing and scanning several samples with different  $T_1$  to compute the RARE SI model.<sup>23</sup> This also improved the accuracy of the model by essentially eliminating possible imprecisions introduced by measurements, especially at low FAs where SIs corresponding to different  $T_1$ s are closer to each other. We found using EPG simulations that the *hybrid* and *sensitivity methods* yielded the same results, up to a constant factor. Imperfections originating from a measured model

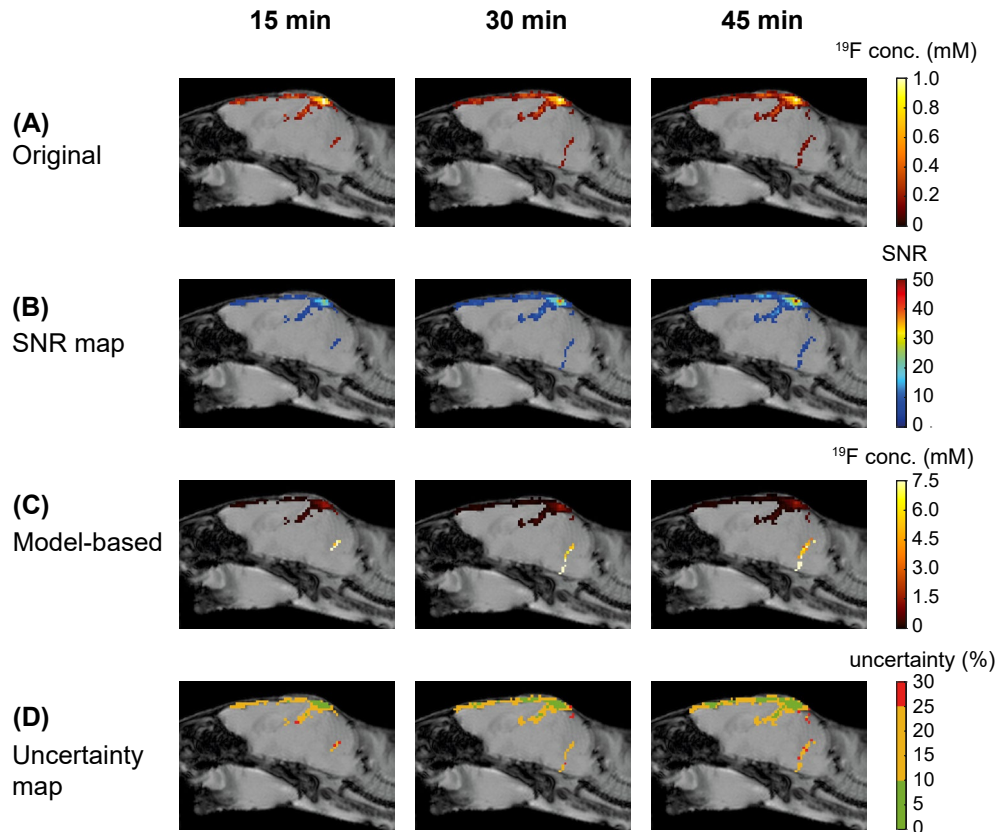


**FIGURE 8** In vivo EAE mouse 2 (score = 1.5) in sagittal orientation. (A) Concentration maps of original images present signals in the meninges as well as in deeper regions of the brain, indicating increased inflammatory cell accumulation. (B) The SNR maps show high SNR at pixels at the top of the mouse head and a reduced SNR in regions distant to the RF probe. (C) After applying the *model-based  $B_1$  correction*, concentration maps show an expected reduction in  $^{19}\text{F}$  concentration in the meninges and an increase in pixels far from the CRP surface. (D) Corresponding uncertainty maps demonstrate the reliability of the  $B_1$ -corrected concentration maps, with most pixels indicating green (uncertainty  $\leq 10\%$ ) and orange ( $10\% < \text{uncertainty} \leq 25\%$ ) values

instead of EPG simulations disturb the symmetry underlying this degeneracy, leading to slight differences between the *hybrid* and *sensitivity methods*. This demonstrates that simulations have a clear advantage, which we expect would also be true for other MR sequences lacking closed-form SI equations.

The use of higher ETLs to further improve SNR through signal averaging produced ghosting artifacts in uniform phantoms (in test images, but also images used for *sensitivity correction*) in regions where  $^{19}\text{F}$  signal was lower. This effect has been widely recognized<sup>45,46</sup> and produced an abnormal increase of signal with the *sensitivity method* in regions adjacent to the artifact, which could not be removed even when changing the phase-encoding direction. The *model-based correction* was affected to a lesser extent (test images still showed ghosting artifacts), since this correction uses FA and  $B_1^-$  maps computed with FLASH images. This was observed when correcting the uniform phantom in which the *model-based correction* yielded MAPEs lower than 25% for all ROIs, and calculated PIUs were equally higher than those achieved with the *sensitivity method*.

Therefore, we conclude that the *model-based correction method* is more robust than the *sensitivity method*, which poses some constraints in MR scanning parameters.

Furthermore, the uniform phantom was prepared with  $^{19}\text{F}$  concentration (0.2 mM) and SNR (range 50 to 0) comparable to those achieved in EAE mice administered with PFCE-NPs (maximum  $^{19}\text{F}$  concentration 2 mM, SNR between 50 and 0 in all cases). Because in transceive surface RF probes the SNR is much higher when close to the RF probe, the  $B_1$  correction approach and uncertainty propagation model were assessed in realistic scenarios and validated for low SNRs far away from the RF probe (Figure 5F–I).

Reference caps placed above the phantoms or mouse heads were developed to allow for reference power calibrations. Little extra time was needed to acquire separate reference images to compute  $^{19}\text{F}$  concentrations. Furthermore, individual  $B_1$  maps were measured to correct more pixels in the reference caps, since the wall thickness of the 15-mL tube (0.8 mm) excluded more than half of the pixels of the reference. Corrections of the reference caps were nevertheless of poorer quality, with  $B_1$  inhomogeneities at the sides.

This was expected due to the large gradient close to the probe surface. Also, reference power adjustments may not be reliable in the close slices, further demonstrating that FA calibration is non-trivial and could be improved.<sup>42,47</sup>

Reliable  $B_1$  correction is indispensable for robustly quantifying the  $^{19}\text{F}$  signal when using the  $^{19}\text{F}$ -CRP in studies using  $^{19}\text{F}$ -NPs to measure the inflammatory burden in EAE in vivo. In this study we presented two EAE animals with discrepancies between  $^{19}\text{F}$  signal and clinical score: the animal with lower clinical severity showed more  $^{19}\text{F}$  signal. This reflects the clinico-radiological paradox, well described in MS<sup>48</sup> and EAE,<sup>49</sup> whereby clinical status and radiological findings diverge, underscoring the urgent need to establish more quantitative MRI methods to assess disease severity objectively, such as that presented in the current study.

We performed Monte Carlo SNR simulations to estimate SI quantification uncertainties. Simulations were designed to include a wide SNR range (Table 2), taking into account the typically low SNR values for  $^{19}\text{F}$  (SNR = 0–10 in 0.5 steps) as well as higher SNRs (SNR up to 1500). We found that concentration uncertainty maps yielded a linear dependence of the uncertainty on SNR, with constant regions ( $\leq 10\%$  with SNR  $\geq 10.1$  and  $\leq 25\%$  when SNR  $\geq 4.25$ ). This is consistent with the results previously demonstrated for  $^1\text{H}$  imaging, in which SNR was not limited. These SNR requirements are highly relevant for the experimental implementation of our approach and aim to guide other researchers to balance scan time with the uncertainty of the quantification of low-SNR  $^{19}\text{F}$  RARE-MRI applications.

To examine the accuracy of  $B_1$ -corrected ex vivo concentration maps, these were compared to those obtained with a volume resonator. Despite the best efforts to select an identical anatomical position with both volume resonators, minor differences in  $^1\text{H}$  might cause slight changes in the visible  $^{19}\text{F}$  signal. Nevertheless, there was overall good agreement in  $^{19}\text{F}$  features and corresponding concentrations, confirmed by the computed uncertainty maps. In vivo error concentration maps showed positive results even when SNR values achieved were significantly lower than ex vivo, due to reduced scan times. Future studies using 3D-RARE combined with accelerated acquisition could help further improve concentration errors.<sup>50,51</sup> Moreover, adiabatic pulses could be an interesting addition to 3D-RARE acquisitions to further improve  $B_1^+$ -field uniformity up to a certain region.<sup>52,53</sup> A subsequent *model-based  $B_1$  correction* could be of value to increase the  $B_1$ -corrected area.

To conclude, we demonstrated a workflow that allows  $^{19}\text{F}$  signal quantification using a *model-based  $B_1$  correction method* together with a single-tuned transceive surface RF probe and RARE. We also highlight several issues that should be considered when performing similar studies. This approach remarkably improved concentration errors from  $> 100\%$  to  $< 25\%$ .  $B_1$  correction methods will

be critical to ensure that the detected  $^{19}\text{F}$  signal depends exclusively on  $^{19}\text{F}$  spin density and not on distance to the RF probe surface, while utilizing the SNR benefit provided by  $^{19}\text{F}$ -CRPs. These results are particularly promising for future clinical applications,<sup>54–57</sup> in which the lower SNR achieved at clinical field strengths necessitates the use of transceive surface RF probes.

## ACKNOWLEDGMENT

The authors thank Rui Pedro A. G. Teixeira (Perspectum, Oxford, United Kingdom), João S. Periquito (Max-Delbrück-Center for Molecular Medicine in the Helmholtz Association, Berlin, Germany and Charité Universitätsmedizin-Berlin), and Andreia C. de Freitas (Instituto Superior Técnico, Lisbon, Portugal) for the helpful discussions about EPG simulations and RARE imaging, and Matthias Weigel (University of Basel, Basel, Switzerland) for generously providing his EPG simulation code. Open access funding enabled and organized by ProjektDEAL.

## CONFLICT OF INTEREST

Andre Kuehne, Alonso Vázquez and Helmar Waiczies are employees of MRI.TOOLS, Berlin, Germany. Thoralf Niendorf is founder and CEO of MRI.TOOLS. Andreas Pohlmann is currently an employee of Siemens Healthineers. All other authors declare no conflict of interest.

## DATA AVAILABILITY STATEMENT

The code and data that support the findings of this study will be openly available in GitHub at [https://github.com/pramosdelgado/B1correction\\_for\\_19F](https://github.com/pramosdelgado/B1correction_for_19F).

## ORCID

Paula Ramos Delgado  <https://orcid.org/0000-0003-2009-3024>  
 Andre Kuehne  <https://orcid.org/0000-0002-4133-5056>  
 Mariya Aravina  <https://orcid.org/0000-0002-0970-6080>  
 Jason M. Millward  <https://orcid.org/0000-0003-4484-2798>  
 Alonso Vázquez  <https://orcid.org/0000-0002-0725-3698>  
 Ludger Starke  <https://orcid.org/0000-0002-0359-0101>  
 Helmar Waiczies  <https://orcid.org/0000-0001-6651-4790>  
 Andreas Pohlmann  <https://orcid.org/0000-0002-8572-2568>  
 Thoralf Niendorf  <https://orcid.org/0000-0001-7584-6527>  
 Sonia Waiczies  <https://orcid.org/0000-0002-9916-9572>

## TWITTER

Paula Ramos Delgado  @pramosdelgado

## REFERENCES

- Ruiz-Cabello J, Barnett B, Bottomley P, Bulte J. Fluorine ( $^{19}\text{F}$ ) MRS and MRI in biomedicine. *NMR Biomed.* 2011;24:114–129.
- Waiczies S, Ji Y, Niendorf T. Tracking methods for dendritic cells. In: Flögel U, Ahrens E, eds. *Fluorine Magnetic Resonance Imaging*. Pan Stanford Publishing; 2017:243–281.

3. Chen J, Lanza G, Wickline S. Quantitative magnetic resonance fluorine imaging: today and tomorrow. *Wiley Interdiscip Rev Nanomed Nanobiotechnol.* 2015;2:431-440.
4. Axel L, Hayes C. Surface coil magnetic resonance imaging. *Archives Internationales De Physiologie Et De Biochimie.* 1985;93:11-18.
5. Ratering D, Baltes C, Nordmeyer-Massner J, Marek D, Rudin M. Performance of a 200-MHz cryogenic RF probe designed for MRI and MRS of the murine brain. *Magn Reson Med.* 2008;59:1440-1447.
6. Baltes C, Radzwill N, Bosshard S, Marek D, Rudin M. Micro MRI of the mouse brain using a novel 400 MHz cryogenic quadrature RF probe. *NMR Biomed.* 2009;22:834-842.
7. Kovacs H, Moskau D, Spraul M. Cryogenically cooled probes—a leap in NMR technology. *Prog Nucl Magn Reson Spectrosc.* 2005;46:131-155.
8. Waiczies S, Millward JM, Starke L, et al. Enhanced fluorine-19 MRI sensitivity using a cryogenic radiofrequency probe: technical developments and *ex vivo* demonstration in a mouse model of neuroinflammation. *Sci Rep.* 2017;7:9808.
9. Sack M, Wetterling F, Sartorius A, Ende G, Weber-Fahr W. Signal-to-noise ratio of a mouse brain <sup>13</sup>C CryoProbe™ system in comparison with room temperature coils: spectroscopic phantom and *in vivo* results. *NMR Biomed.* 2014;27:709-715.
10. Khalil AA, Mueller S, Foddiss M, et al. Longitudinal <sup>19</sup>F magnetic resonance imaging of brain oxygenation in a mouse model of vascular cognitive impairment using a cryogenic radiofrequency coil. *Magn Reson Mater Phys, Biol Med.* 2019;32:105-114.
11. Collins CM, Webb AG. Quadrature surface coils. In: Harris RK, Wasylishen RL, eds. *eMagRes.* Hoboken, NJ: John Wiley & Sons, Ltd; 2010. <https://doi.org/10.1002/9780470034590.emrstm1115>
12. Hoult D, Chen C, Sank V. Quadrature detection in the laboratory frame. *Magn Reson Med.* 1984;1:339-353.
13. Glover G, Hayes C, Pelc N, et al. Comparison of linear and circular polarization for magnetic resonance imaging. *J Magn Reson.* 1985;64:255-270.
14. Peshkovsky AS, Kennan RP, Fabry ME, Avdievich NI. Open half-volume quadrature transverse electromagnetic coil for high-field magnetic resonance imaging. *Magn Reson Med.* 2005;53:937-943.
15. Schnell M, Subramanian V, Leigh J, Chance B. A new double-tuned probed for concurrent <sup>1</sup>H and <sup>31</sup>P NMx. *J Magn Reson.* 1985;65:122-129.
16. Meyerspeer M, Roig ES, Gruetter R, Magill AW. An improved trap design for decoupling multinuclear RF coils. *Magn Reson Med.* 2014;72:584-590.
17. Crowley M, Evelhoch J, Ackermann J. The surface-coil NMR receiver in the presence of homogeneous B<sub>1</sub> excitation. *J Magn Reson.* 1985;64:20-31.
18. Collewet G, Davenel A, Toussaint C, Akoka S. Correction of intensity nonuniformity in spin-echo T<sub>1</sub>-weighted images. *Magn Reson Imaging.* 2002;20:365-373.
19. Vernikouskaya I, Pochert A, Lindén M, Rasche V. Quantitative <sup>19</sup>F MRI of perfluoro-15-crown-5-ether using uniformity correction of the spin excitation and signal reception. *Magn Reson Mater Phys, Biol Med.* 2019;32:25-36.
20. Wang J, Qiu M, Constable R. *In vivo* method for correcting transmit/receive nonuniformities with phased array coils. *Magn Reson Med.* 2005;53:666-674.
21. Meara S, Barker G. Evolution of the longitudinal magnetization for pulse sequences using a fast spin-echo readout: application to fluid-attenuated inversion-recovery and double inversion-recovery sequences. *Magn Reson Med.* 2005;54:241-245.
22. Conturo T, Beth A, Arenstorf R, Price R. Simplified mathematical description of longitudinal recovery in multiple-echo sequences. *Magn Reson Med.* 1987;4:282-288.
23. Ramos Delgado P, Kuehne A, Periquito J, et al. B<sub>1</sub> inhomogeneity correction of RARE MRI with transceive surface radiofrequency probes. *Magn Reson Med.* 2020;84:2684-2701.
24. Constantinescu C, Farooqi N, O'Brien K, Gran B. Experimental autoimmune encephalomyelitis (EAE) as a model for multiple sclerosis (MS). *Br J Pharmacol.* 2011;164:1079-1106.
25. Robinson A, Harp C, Noronha A, Miller S. The experimental autoimmune encephalomyelitis (EAE) model of MS: utility for understanding disease pathophysiology and treatment. In: Goodin D, ed. *Handbook of Clinical Neurology*, vol. 122. Elsevier BV; 2014:173-189.
26. Waiczies H, Lepore S, Drechsler S, et al. Visualizing brain inflammation with a shingled-leg radio-frequency head probe for <sup>19</sup>F/<sup>1</sup>H MRI. *Sci Rep.* 2013;3:1280.
27. Waiczies S, Lepore S, Sydow K, et al. Anchoring dipalmitoyl phosphoethanolamine to nanoparticles boosts cellular uptake and fluorine-19 magnetic resonance signal. *Sci Rep.* 2015;5:8427.
28. Waiczies H, Lepore S, Janitzek N, et al. Perfluorocarbon particle size influences magnetic resonance signal and immunological properties of dendritic cells. *PLoS One.* 2011;6:e21981.
29. Starke L, Niendorf T, Waiczies S. Data preparation protocol for low signal-to-noise ratio fluorine-19 MRI. In: Pohlmann A, Niendorf T, eds. *Preclinical MRI of the Kidney: Methods and Protocols.* Springer US; 2021:711-722.
30. Henkelman R. Measurement of signal intensities in the presence of noise in MR images. *Med Phys.* 1985;12:232-233.
31. Weigel M. Extended phase graphs: dephasing, RF pulses, and echoes—pure and simple. *J Magn Reson Imaging.* 2015;41:266-295.
32. Hennig J. Echoes—how to generate, recognize, use or avoid them in MR-imaging sequences. Part I: fundamental and not so fundamental properties of spin echoes. *Concepts Magn Reson.* 1991;3:125-143.
33. Hennig J. Echoes—how to generate, recognize, use or avoid them in MR-imaging sequences. Part II: echoes in imaging sequences. *Concepts Magn Reson.* 1991;3:179-192.
34. Zhang J. Modern Monte Carlo methods for efficient uncertainty quantification and propagation: a survey. *Wiley Interdiscip Rev Comput Stat.* 2020;13:e1539.
35. Kroese D, Rubinstein R. Monte Carlo methods. *Wiley Interdiscip Rev Comput Stat.* 2012;4:48-58.
36. Price R, Axel L, Morgan T, et al. Quality assurance methods and phantoms for magnetic resonance imaging: report of AAPM nuclear magnetic resonance Task Group No. 1. *Med Phys.* 1989;17:287-295.
37. Jacoby C, Temme S, Mayenfels F, et al. Probing different perfluorocarbons for *in vivo* inflammation imaging by <sup>19</sup>F MRI: image reconstruction, biological half-lives and sensitivity. *NMR Biomed.* 2013;27:261-271.
38. Prinz C, Ramos Delgado P, Eigentler T, Starke L, Niendorf T, Waiczies S. Toward <sup>19</sup>F magnetic resonance thermometry: spin-lattice and spin-spin relaxation times and temperature dependence of fluorinated drugs at 9.4 T. *Magn Reson Mater Phys, Biol Med.* 2018;32:51-61.
39. *Nhist Function [computer program].* Version 1.13.0.0. File Exchange: The MathWorks; 2015.

40. Holland G, Bottomley P, Hinshaw W.  $^{19}\text{F}$  magnetic resonance imaging. *J Magn Reson*. 1977;28:133-136.
41. Ahrens E, Flores R, Xu H, Morel P. In vivo imaging platform for tracking immunotherapeutic cells. *Nat Biotechnol*. 2005;23:983-987.
42. Goette M, Lanza G, Caruthers S, Wickline S. Improved quantitative  $^{19}\text{F}$  MR molecular imaging with flip angle calibration and  $B_1$ -mapping compensation. *J Magn Reson Imaging*. 2015;42:488-494.
43. Constantinides C, Maguire M, McNeill E, et al. Fast, quantitative, murine cardiac  $^{19}\text{F}$  MRI/MRS of PFCE-labeled progenitor stem cells and macrophages at 9.4T. *PLoS One*. 2018;13:e0190558.
44. Kadayakkara D, Damodaran K, Hitchens T, Bulte J, Ahrens E.  $^{19}\text{F}$  spin-lattice relaxation of perfluoropolyethers: dependence on temperature and magnetic field strength (7.0–14.1 T). *J Magn Reson*. 2014;242:18-22.
45. Zhou X, Liang Z, Cofer G, Beaulieu C, Suddarth S, Johnson G. Reduction of ringing and blurring artifacts in fast spin-echo imaging. *J Magn Reson Imaging*. 1993;3:803-807.
46. Mulkern R, Wong S, Winalski C, Jolesz F. Contrast manipulation and artifact assessment of 2D and 3D RARE sequences. *Magn Reson Imaging*. 1990;8:557-566.
47. Schulte RF, Sacolick L, Deppe MH, et al. Transmit gain calibration for nonproton MR using the Bloch-Siegert shift. *NMR Biomed*. 2010;24:1068-1072.
48. Barkhof F. The clinico-radiological paradox in multiple sclerosis revisited. *Curr Opin Neurol*. 2002;15:239-245.
49. Wuerfel J, Tysiak E, Prozorovski T, et al. Mouse model mimics multiple sclerosis in the clinico-radiological paradox. *Eur J Neurosci*. 2007;26:190-198.
50. Zhong J, Mills P, Hitchens T, Ahrens E. Accelerated fluorine-19 MRI cell tracking using compressed sensing. *Magn Reson Med*. 2013;69:1683-1690.
51. Darçot E, Yerly J, Hilbert T, et al. Compressed sensing with signal averaging for improved sensitivity and motion artifact reduction in fluorine-19 MRI. *NMR Biomed*. 2021;34:e4418.
52. Zhou X. Adiabatic radiofrequency pulses. In: Bernstein M, King K, Zhou X, eds. *Handbook of MRI Pulse Sequences*. Elsevier Academic Press; 2004:177-212.
53. de Graaf R, Rothman D, Behar K. Adiabatic RARE imaging. *NMR Biomed*. 2003;16:29-35.
54. Ahrens E, Helfer B, O'Hanlon C, Schirda C. Clinical cell therapy imaging using a perfluorocarbon tracer and fluorine-19 MRI. *Magn Reson Med*. 2014;72:1696-1701.
55. Amiri H, Srinivas M, Veltien A, van Uden M, de Vries I, Heerschap A. Cell tracking using ( $^{19}\text{F}$ ) magnetic resonance imaging: technical aspects and challenges towards clinical applications. *Eur Radiol*. 2015;25:726-735.
56. Chapelin F, Capitini C, Ahrens E. Fluorine-19 MRI for detection and quantification of immune cell therapy for cancer. *J Immunotherapy Cancer*. 2018;6:105.
57. Fox M, Gaudet J, Foster P. Fluorine-19 MRI contrast agents for cell tracking and lung imaging. *Magn Reson Insights*. 2016;22:53-67.

## SUPPORTING INFORMATION

Additional supporting information may be found in the online version of the article at the publisher's website.

**FIGURE S1** Exemplary spectra used for  $T_1$  calculation for (A) reference cap containing 24mM  $^{19}\text{F}$ -loaded NPs

(non-localized spectroscopy), (B) ex vivo CNS of an EAE mouse with administered  $^{19}\text{F}$ -loaded NPs prior to perfusion (PRESS), and (C) in vivo mouse with active EAE and administered  $^{19}\text{F}$ -loaded NPs (PRESS). Measurements were performed using a  $^1\text{H}/^{19}\text{F}$  volume resonator. Selected TR = 10000 ms

**FIGURE S2** Ex vivo phantom (score=2.0) in axial orientation for increasing scan times (15 minutes, 1 hour, 3 hours and 6 hours). Reference images (A) acquired with the  $^1\text{H}/^{19}\text{F}$  volume resonator show less  $^{19}\text{F}$  signal in the brain compared to  $^{19}\text{F}$ -CRP images (B). The steep gradient in  $B_1$  field of the  $^{19}\text{F}$ -CRP prevents from detecting the prominent lymph node signals in contrast to the volume resonator. SNR maps for the CRP images are presented in (C).  $B_1$ -corrected images show concentration values closer to the reference obtained with the volume resonator (D). Uncertainty maps (E) reveal the reliability of the  $B_1$ -corrected concentration maps, with most pixels indicating green (uncertainty  $\leq 10\%$ ) and orange ( $10\% < \text{uncertainty} \leq 25\%$ ) values

**FIGURE S3** In vivo EAE mouse 1 (score = 2.5) in axial orientation. Concentration maps of original images (A) show an initial overestimation of the  $^{19}\text{F}$  concentration in regions close to the RF probe surface (e.g. meninges) which partly correspond with regions with high SNR (B). After performing the *model-based  $B_1$  correction* (C),  $^{19}\text{F}$  concentration maps are computed. Their reliability is presented by the uncertainty maps (D) which show green (uncertainty  $\leq 10\%$ ) and orange ( $10\% < \text{uncertainty} \leq 25\%$ ) values for most pixels

**FIGURE S4** In vivo EAE mouse 2 (score = 1.5) in axial orientation. (A) Concentration maps of original images present signals in the meninges as well as in deeper regions of the brain, indicating increased inflammatory cell accumulation. (B) SNR maps show high SNR at pixels at the top of the mouse head and a reduced SNR in regions distant to the RF probe. After applying the *model-based  $B_1$  correction* (C), concentration maps show an expected reduction in  $^{19}\text{F}$  concentration in the meninges and an increase in pixels far from the CRP surface. Corresponding uncertainty maps (D) demonstrate the reliability of the  $B_1$ -corrected concentration maps, with most pixels indicating green (uncertainty  $\leq 10\%$ ) and orange ( $10\% < \text{uncertainty} \leq 25\%$ ) values

**How to cite this article:** Ramos Delgado P, Kuehne A, Aravina M, et al.  $B_1$  inhomogeneity correction of RARE MRI at low SNR: Quantitative in vivo  $^{19}\text{F}$  MRI of mouse neuroinflammation with a cryogenically-cooled transceive surface radiofrequency probe. *Magn Reson Med*. 2022;87: 1952–1970. doi:[10.1002/mrm.29094](https://doi.org/10.1002/mrm.29094)